ACS Photonics

Article

pubs.acs.org/journal/apchd5

Electron Energy-Loss Spectroscopy Calculation in Finite-Difference Time-Domain Package

Yang Cao,[†,‡] Alejandro Manjavacas,*[,†,‡] Nicolas Large,*[,‡,§,∥] and Peter Nordlander*[,†,§]

[†]Department of Physics and Astronomy, [§]Department of Electrical and Computer Engineering, and [‡]Laboratory for Nanophotonics, Rice University, 6100 Main Street, Houston, Texas 77005, United States

Supporting Information

ABSTRACT: Electron energy-loss spectroscopy (EELS) is a unique tool that is extensively used to investigate the plasmonic response of metallic nanostructures. We present here a novel approach for EELS calculations using the finite-difference time-domain (FDTD) method (EELS-FDTD). We benchmark our approach by direct comparison with results from the well-established boundary element method (BEM) and published experimental results. In particular, we compute EELS spectra for spherical nanoparticles, nanoparticle dimers, nanodisks supported by various substrates, and a gold bowtie antenna on a silicon nitride substrate. Our EELS-FDTD method can be easily extended to more complex geometries and configurations. This implementation can also be directly exported beyond the FDTD framework and implemented in other Maxwell's equation solvers.

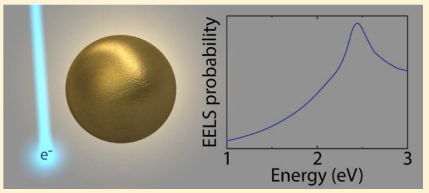

KEYWORDS: *numerical recipe, electron energy-loss spectroscopy (EELS), finite-difference time-domain (FDTD), plasmonic nanostructures, gold nanoparticle, silver dimer, gold nanodisk, bowtie antennas*

Energy-loss spectroscopy using fast electrons was used in the first experimental detection of surface plasmons in metals.[1−4] Since these pioneering studies, electron energy-loss spectroscopy (EELS) has become a unique tool for probing surface plasmons of metallic nanostructures with unprecedented spatial (<1 nm) and energy (<100 meV) resolution.[5−10] With the ability of electrons to probe dark surface plasmons,[10−13] to provide accurate information on the nanostructure morphology and local environment,[5] quantitative information on surface plasmon kinetics, damping, and dispersion,[4,14] EELS has become an irreplaceable tool for the experimental study of surface plasmons. Consequently, EELS is widely used to investigate optical properties of complex metallic nanostructures (i.e., complicated geometries, strongly coupled nanosystems).[9] The particular nature of the electromagnetic field of an electron (i.e., fast moving point charge, Figure 1a) makes the theoretical modeling of EELS data more involved than the modeling of optical experiments. For such simulations a myriad of different numerical techniques have been developed in the past years, including boundary element method (BEM),[15,16] discrete dipole approximation (DDA),[17−19] finite-element method (FEM),[10,12,20] finite-difference time-domain (FDTD) method,[21] and discontinuous Galerkin time-domain (DGTD) method.[22] Although these methods are able to predict and interpret experimental EELS spectra, they possess some of the following significant drawbacks: (i) the need for large computational resources,[17−19] (ii) limitations to nonpenetrating electron trajectories,[18−20,22] (iii) requiring highly symmetrical geometries,[15−19] and (iv) complexity (i.e., programming skills required, absence of user-friendly interface).[15−22] These drawbacks are the main reason why EELS experimental results are generally compared to numerical simulations with optical excitations.[11,23−25] A recently published review article by Kociak and Stéphan explicitly states that, despite an implementation for cathodoluminescence (CL) spectroscopy in FDTD[26−28] and the EELS implementation in DGTD,[22] there is a clear lack of time-domain numerical methods for electron-beam spectroscopy calculations.[6]

In this paper, we propose a novel numerical procedure for EELS simulations employing a reliable and widely used commercial package: Lumerical FDTD Solutions.[29] This package implements a high performance 3D solver that offers a user-friendly environment for solving Maxwell's equations using the FDTD method.[30] We benchmark our method by direct comparison with results from the well-established BEM method[15] for three representative systems: (i) isolated nanospheres, (ii) nanosphere dimers, and (iii) nanodisks supported by a substrate. In the particular case of nonpenetrating trajectories for nanospheres, we also compare our method with analytical results from Mie theory.[9,31,32] Finally, in order to demonstrate the power of this implementation, we perform EELS calculations for a more complex geometry consisting of a supported bowtie antenna where experimental results are available.

METHOD

The theoretical formalism for EELS simulations has been extensively discussed in the literature (cf. refs 1, 9, and references therein). The physics of EELS can be understood as follows: the electric field produced by an electron moving with constant velocity **v** polarizes the nanostructure placed in the

Received: October 30, 2014
Published: February 16, 2015

DOI: 10.1021/ph500408e
ACS Photonics 2015, 2, 369−375

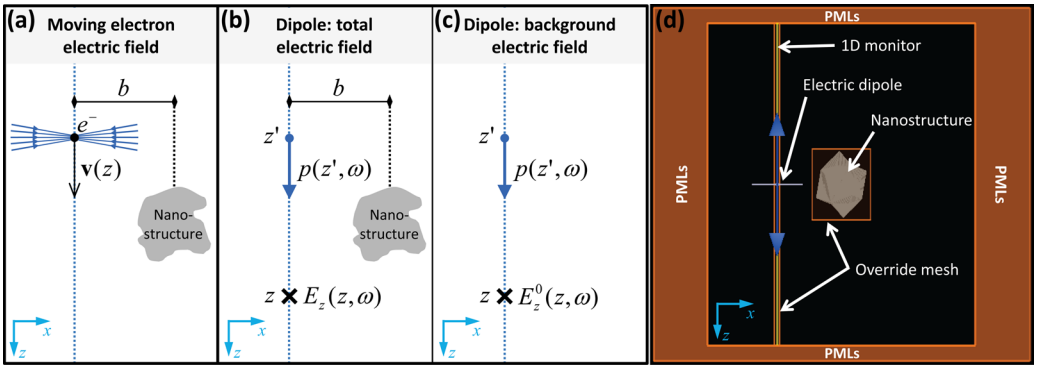

Figure 1. Description of the geometry employed to calculate the electron energy-loss spectrum. (a) Schematics showing the electric field of an electron moving with velocity **v** along a straight-line trajectory separated from a metallic nanostructure by the impact parameter b. (b, c) Geometry used to calculate the induced electric field $E_z^{\mathrm{ind}}(z,\omega) = E_z(z,\omega) - E_z^0(z,\omega)$ for a nanostructure. Here E_z and E_z^0 represent the z-component of the electric field generated by an electric dipole $p(z',\omega)$ at position z in presence and in absence of the metallic nano-object, respectively. (d) FDTD simulation setup showing (i) the FDTD simulation domain with PML boundary conditions, (ii) the nanostructure geometry, (iii) the electric dipole source, (iv) the 1D monitor used to record the electric field along the electron path, and (v) the override meshes used to improve the discretization for the nanostructure and the electron trajectory.

vicinity of its trajectory (cf. Figure 1a). This, in turn, induces an electric field $\mathbf{E}^{\mathrm{ind}}$ that acts back on the electron, exerting a force that produces the energy loss. This energy loss can be written as[9]

$$\Delta E_{\mathrm{EELS}} = e\int \mathbf{v}\cdot\mathbf{E}^{\mathrm{ind}}[\mathbf{r}_e(t),\, t]\mathrm{d}t = \int_0^\infty \hbar\omega\Gamma_{\mathrm{EELS}}(\omega)\mathrm{d}\omega$$

where e is the elementary charge, $\mathbf{r}_e(t)$ represents the electron trajectory, and

$$\Gamma_{\mathrm{EELS}}(\omega) = \frac{e}{\pi\hbar\omega}\int \mathrm{Re}\{e^{-i\omega t}\mathbf{v}\cdot\mathbf{E}^{\mathrm{ind}}[\mathbf{r}_e(t),\, \omega]\}\mathrm{d}t + \Gamma_{\mathrm{bulk}}(\omega) \tag{1}$$

is the energy loss probability per unit of frequency ω.[9] The second term of this expression, Γ_{bulk}, represents the bulk loss probability. This contribution can be calculated using the following analytical expression[9]

$$\Gamma_{\mathrm{bulk}} = \frac{e^2L}{\pi\hbar v^2}\mathrm{Im}\left\{\left(\frac{v^2}{c^2} - \frac{1}{\varepsilon}\right)\ln\left(\frac{c^2q_c^2/\omega^2 - \varepsilon}{c^2/v^2 - \varepsilon}\right)\right\}$$

where L is the length of the electron trajectory inside the medium, ε is the medium dielectric permittivity, and $q_c \approx \hbar^{-1}[(m_e v\phi_{\mathrm{out}})^2 + (\hbar\omega/v)^2]^{1/2}$ is the cutoff momentum determined by the electron mass m_e, the electron velocity v, and the collection angle ϕ_{out} of the microscope. This expression is valid within the local response approximation, in which only low enough momentum transfers below q_c are collected. In the remainder of this paper, we do not consider the bulk contribution. In addition, and without loss of generality, we assume the electron trajectory to be in the (x,z) plane, parallel to z-axis, and separated from the origin by the impact parameter b, so $\mathbf{v} = v\hat{\mathbf{z}}$ and $\mathbf{r}_e(t) = (b,0,vt)$.

The electric field created by an arbitrary current distribution (such as a beam of electrons) can be written as[33]

$$\mathbf{E}[\mathbf{r}(t),\, \omega] = -4\pi i\omega\int \mathbf{G}(\mathbf{r},\, \mathbf{r}',\, \omega)\mathbf{j}(\mathbf{r}',\, \omega)\mathrm{d}\mathbf{r}' \tag{2}$$

in terms of the Green tensor of Maxwell's equations $\mathbf{G}(\mathbf{r},\mathbf{r}',\omega)$ (note that we use Gaussian units). This quantity is defined as the solution of

$$\left[-\nabla\times\nabla\times + \varepsilon(\mathbf{r},\, \omega)\frac{\omega^2}{c^2}\right]\mathbf{G}(\mathbf{r},\, \mathbf{r}',\, \omega) = \frac{1}{c^2}\delta(\mathbf{r} - \mathbf{r}')\mathbf{I}$$

where $\varepsilon(\mathbf{r},\omega)$ is the permittivity of the medium and $\mathbf{I}$ is the unit tensor. Using the electron current density relevant for EELS $\mathbf{j}(\mathbf{r}',\omega) = -e\delta(x - b)\delta(y)e^{i\omega z/v}\hat{\mathbf{z}}$ and eq 2 we can rewrite the loss probability (eq 1) as[9]

$$\Gamma_{\mathrm{EELS}}(\omega) = \frac{4e^2}{\hbar}\int\int_{-\infty}^{\infty}\cos\left[\frac{\omega(z - z')}{v}\right] \times \mathrm{Im}[-G_{zz}^{\mathrm{ind}}(z,\, z',\, \omega)]\mathrm{d}z\mathrm{d}z' \tag{3}$$

Here, $G_{zz}^{\mathrm{ind}}(z,z',\omega) = \hat{\mathbf{z}}\cdot[\mathbf{G}(z,z',\omega) - \mathbf{G}^0(z,z',\omega)]\cdot\hat{\mathbf{z}}$, with $\mathbf{G}^0(\mathbf{r},\mathbf{r}',\omega)$ being the Green tensor for vacuum (to simplify the notation we have omitted the lateral spatial coordinates $x = b$ and $y = 0$ in the arguments of the Green functions and related quantities). In the derivation of this expression, we have also used the reciprocity property of the Green tensor $\mathbf{G}(\mathbf{r},\mathbf{r}',\omega) = \mathbf{G}^{\mathrm{T}}(\mathbf{r}',\mathbf{r},\omega)$. Interestingly, $G_{zz}^{\mathrm{ind}}(z,z',\omega)$ can be obtained from the z-component of the electric field induced at position z, by an electric dipole of amplitude $p(z',\omega)$ placed at z' and oriented along z-axis

$$G_{zz}^{\mathrm{ind}}(z,\, z',\, \omega) = -\frac{1}{4\pi\omega^2}\frac{E_z^{\mathrm{ind}}(z,\, \omega)}{p(z',\, \omega)}$$

Using this expression, we can rewrite eq 3 as

$$\Gamma_{\mathrm{EELS}}(\omega) = \frac{e^2}{\pi\hbar\omega^2}\int\int_{-\infty}^{\infty}\cos\left[\frac{\omega(z - z')}{v}\right] \times \mathrm{Im}\left[\frac{E_z^{\mathrm{ind}}(z,\, \omega)}{p(z',\, \omega)}\right]\mathrm{d}z\mathrm{d}z' \tag{4}$$

Therefore, all we need to do in order to obtain the loss probability is to compute the induced electric field generated by an electric dipole along the electron trajectory. Notice that eq 4 involves only the imaginary part of the induced field, which remains finite even at the position of the dipole. The use of the induced field, in place of the total field, for nonpenetrating trajectories is not required by the theoretical formalism, since an electron cannot produce energy loss in absence of material structures. However, due to the finite accuracy of the FDTD

DOI: 10.1021/ph500408e
ACS Photonics 2015, 2, 369−375

calculations we choose to work with the induced field in order to minimize any numerical instability originating from the calculation of the fields. In order to calculate the field, we can employ any Maxwell's equation solver. Here, we choose to work with the commercial software package Lumerical FDTD Solutions[29] due to its convenient user environment. The computation procedure starts by setting a 3D FDTD simulation domain with perfectly matched layers (PMLs) to prevent spurious reflections from outer boundaries (Figure 1b,d).[34] We then insert the nanostructure and define an override mesh that allows us to manually adjust the mesh grid size in a particular region. This allows us to optimize the discretization of the physical object and to improve the convergence. After that, we place a 1D (linear) monitor along the electron trajectory that allows us to calculate the electric field at specific points. The monitor is extended across the entire simulation domain through the PMLs. Again, to improve the convergence and to ensure a proper spatial discretization along the electron trajectory, we place a second override mesh on top of the monitor. Next, we position an electric point dipole $p(z',\omega)$ on the mesh grid points, aligned with the electron path, and successively displace it from mesh point to mesh point along the electron trajectory from $z' = z_{max}$ (upper PML) to $z' = z_{min}$ (lower PML). This electric dipole acts as a source in Maxwell's equations. For each position, we record the z-component of the total electric field $E_z(z,\omega)$ along the entire monitor (Figure 1b). To obtain the induced electric field $E_z^{ind}(z,\omega)$, we subtract the background electric field $E_z^0(z,\omega)$ from $E_z(z,\omega)$. The former quantity is calculated using the previously described protocol but removing all the physical objects (e.g., nano-object and substrate) from the simulation domain (Figure 1c). For situations where the electron trajectory penetrates into the absorbing medium (e.g., the metal), one needs to calculate the corresponding background electric field generated by an electric dipole placed in an infinite space filled with the corresponding material. In practice, this can be accomplished by placing the dipole at the center of a sphere composed of this material, whose diameter must be chosen large enough to minimize the field spill out into the surrounding medium. Here we choose this diameter equal to the monitor length. In metals, as the field of the electric dipole decays to zero after a few tens of nanometers, no field exits the micron-sized metallic domain which, thus, can be considered as infinite from the dipole's point of view. Incidentally, since FDTD simulations are not stable when an absorbing medium is extended through the PMLs, this forces us to enlarge the simulation domain and the monitor to prevent the absorbing medium to reach into the PMLs. Once the induced electric field is calculated, the EELS spectrum is readily computed using eq 4. Lumerical and Matlab scripts used for the postprocessing (i.e., calculation of the induced electric field and calculation of the integral using eq 4) are presented in the Supporting Information, S1. Finally, we note that the velocity of the electron only enters in eq 4 through the cosine function. This allows us to compute EELS spectra for any electron velocity from a single FDTD calculation. It is important to notice that one can either calculate all the dipole positions in one single FDTD calculation or split each dipole position into smaller subcalculations to increase the parallelization and optimization.[29] The results presented in this paper are performed using the later procedure.

ISOLATED NANOSTRUCTURE

We first illustrate the EELS-FDTD implementation for the case of an isolated gold nanosphere of diameter a = 160 nm placed in vacuum. To benchmark our method, BEM calculations are performed using an electron source implemented in the axial-symmetry version of this semianalytical method following the formalism established in ref 15. In addition, the simple spherical geometry allows us to perform analytical (Mie theory).[31] We use the dielectric function of gold tabulated by Johnson and Christy.[35] While the experimental values are used as is in the BEM and Mie calculations, analytical multicoefficient models (MCMs) are used in FDTD to fit these experimental data and overcome the difficulty of adapting spectrally tabulated dielectric permittivities into time-domain methods (cf. Supporting Information, S2).[29] The nanoparticle center is placed at the origin of the coordinate system. To ensure a good convergence (cf. Supporting Information, S3), we set a monitor length of 1500 nm (i.e., $z_{max(min)} = \pm 750$ nm). The other parameters used in the Lumerical FDTD Solutions simulation are set as follows: a simulation time of 100 fs with an auto-shutoff parameter of 10^{-5}, a mesh accuracy of 5 (i.e., 22 mesh points per wavelength), and mesh refinement algorithm set to "conformal variant 0" allowing for a nonuniform mesh over the FDTD domain. The physical meaning of these proprietary parameters is provided in Supporting Information, S3. An initial simulation is performed to calculate the total electric field E_z at each point along the electron trajectory in the frequency range 1−3 eV. A second calculation is then performed for the same electric dipole positions in absence of the nanoparticle to calculate the background electric field generated by the dipole in vacuum E_z^0. Schematics of these two configurations is shown in Figure 1b,c. Then, the induced electric field is computed as $E_z^{ind}(z) = E_z(z) - E_z^0(z)$ and inserted into eq 4 to obtain the EELS spectra. The results of this calculation are shown with blue lines in Figure 2 for three different impact parameters: b = 120 nm (away from the nanoparticle, bottom), b = 82 nm (in close proximity to the nanoparticle, center), and b = 0 nm (through the center of the nanoparticle, top). In all the cases, we use an electron velocity equal to half of the speed of light in vacuum c (i.e., $v = 0.5c$), which corresponds to a kinetic energy of 80 keV.

The results obtained with the EELS-FDTD implementation (blue lines) show a strong peak at 2.4 eV, in very good agreement with BEM (red lines) and Mie theory (black triangles) calculations. This peak corresponds to the quadrupolar mode of the nanoparticle. The dipolar mode of the nanoparticle only appears as a shoulder in the spectrum at smaller energies. Interestingly, the position of this peak depends on the impact parameter due to retardation effects, originating from the frequency dependence of the field from the electron. In contrast to several published methods,[18−20,22] the EELS-FDTD implementation can also handle penetrating trajectories (Figure 2, top). However, for such cases one has to be careful when performing the FDTD simulation.

The relative position of the electric dipoles with respect to the nanoparticle surface can artificially introduce numerical errors. We show in Supporting Information, S5, that when an electric dipole is placed exactly at the nanoparticle surface, it produces an overestimation of the EELS signal. This is easily solved by slightly displacing the entire nanostructure along the z-axis with respect to the monitor mesh grid (typically 1/3 mesh step). The discrepancies observed between FDTD and

DOI: 10.1021/ph500408e
ACS Photonics 2015, 2, 369−375

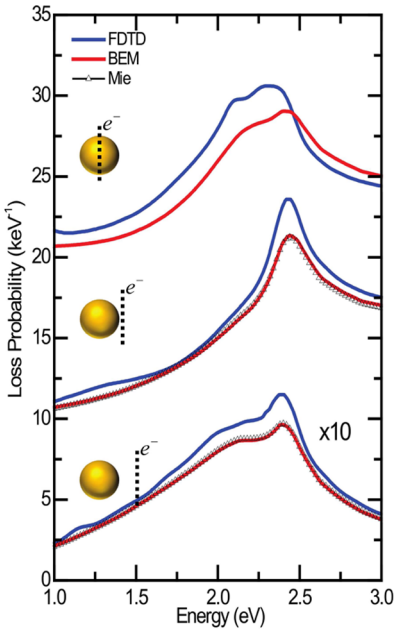

Figure 2. EELS spectra for a gold nanosphere of diameter a = 160 nm calculated with the EELS-FDTD implementation (blue lines) for three impact parameters. From top to bottom: b = 0 nm, b = 82 nm, and b = 120 nm. The EELS-FDTD calculations are compared with BEM calculations (red lines), and with Mie theory (black triangles, only for $b > a/2$). The spectra for b = 120 nm are multiplied by ×10 to improve the clarity of the figure. The electron velocity is taken equal to 0.5c (i.e., 80 keV) in all cases.

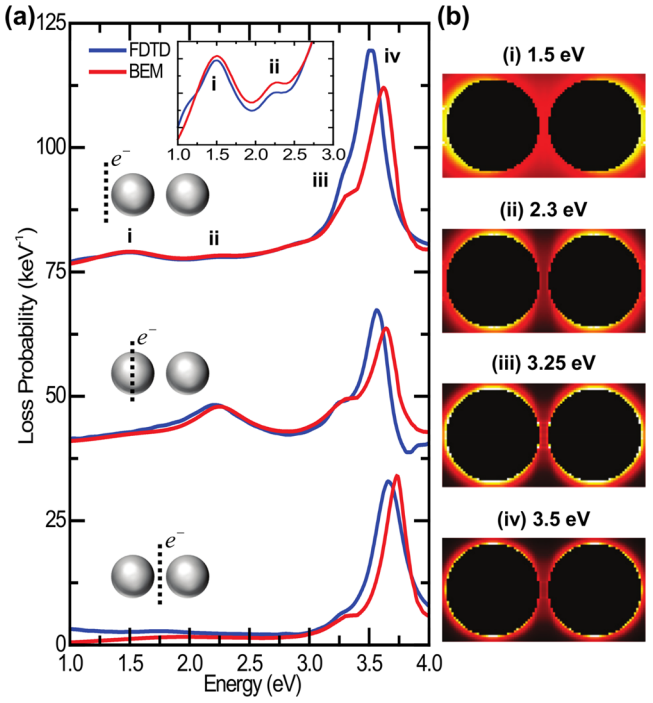

Figure 3. (a) EELS spectra for a dimer of silver nanospheres of diameter a = 160 nm separated by a gap g = 5 nm. Results obtained with the EELS-FDTD implementation (blue lines) are compared with BEM calculations (red lines) for three different impact parameters, from top to bottom: b = 164.5 nm, b = 82.5 nm, and b = 0 nm. In all cases, the electron velocity is fixed to 0.5c (i.e., 80 keV). Inset: Zoom-in view of the low energy part of the upper spectrum. (b) EELS maps calculated at (i) 1.5, (ii) 2.3, (iii) 3.25, and (iv) 3.5 eV.

BEM results (Figure 2, top) can be minimized by increasing the number of dipoles used in the calculation, in particular in the part of the trajectory close to the nanostructure, as shown in Supporting Information, S6.

Although our EELS-FDTD implementation requires performing of a large number of short subcalculations (i.e., one per dipole position), it allows for reaching a better convergence level at lower computational cost than DDA[18] in specific configurations (cf. Figure S4 and Table S2 in the Supporting Information). BEM, due to the axial-symmetry nature of this particular problem, allows the user to perform the same calculation much faster. A comparison of the computational resource used by FDTD, DDA, and BEM to calculate the EELS spectrum for an impact parameter b = 82 nm (Figure 2, center) is provided in Supporting Information, S4. A more general and detailed comparison between the three methods can be found in ref 36.

INTERACTING NANO-OBJECTS

Nanoparticle dimers have been extensively studied using EELS.[11,13,22−24,37,38] For this reason, they constitute another ideal system to benchmark our EELS-FDTD method. Here, we study a dimer of closely spaced (i.e., strongly interacting) silver nanospheres of diameter a = 160 nm placed in vacuum. The gap size is fixed to g = 5 nm, and we use the dielectric function for silver tabulated by Palik[39] in the BEM calculations and MCMs fit of the later in the FDTD calculations (Supporting Information, S2). The other simulation parameters are the same as for the gold nanosphere (cf. Supporting Information, S3).

Figure 3 shows the results obtained with our EELS-FDTD method (blue lines) for three different impact parameters: b = 164.5 nm (dimer end, top), b = 82.5 nm (through the center of one of the NP, center), and b = 0 nm (in the gap, bottom). In all the cases, we use an electron velocity of v = 0.5c (80 keV). It is well-known that for large gaps the nanoparticles interact only weakly and the resulting dimer plasmons are essentially bonding and antibonding combinations of the nanoparticle plasmons of the same multipole order (e.g., l = 1, dipole).[40] Here, due to the very small gap-to-diameter ratio (g/a = 0.03), the plasmon modes of the dimer contain contributions from all multipole orders. When the electrons pass in close proximity to the dimer end (upper spectra), both FDTD and BEM show the appearance of two weak localized surface plasmon resonances (LSPRs) at 1.5 and 2.3 eV and stronger features at 3.25 and 3.5 eV (i, ii, iii, and iv, respectively). Though mixed with higher values of l, the 3.5 eV is dominated by the antibonding dipole, while the 3.25 eV feature results from the strong hybridization of high order modes. The low energy and weak features observed at 1.5 and 2.3 eV are the longitudinal and transverse bonding dipole modes, respectively. The EELS maps associated with the four LSPRs (i−iv) are shown in Figure 3b with a 4 nm spatial resolution. For the sake of simplicity and for computational considerations, we here excluded penetrating trajectories. Although the present dimer is much larger (i.e., more retardation effects) and has a smaller gap-to-diameter ratio (i.e., more hybridization), the results are in good agreement with EELS measurements reported in literature.[11,23,24,37,38] The large energy splitting between the bonding and antibonding dipolar LSPRs is the signature of a strong coupling.[37,38,40] When the electron beam follows a penetrating trajectory (center spectra) the high energy antibonding dipole

DOI: 10.1021/ph500408e
ACS Photonics 2015, 2, 369−375

(3.5 eV) remains strong and the transverse bonding dipole (2.3 eV) is strengthened. For a penetrating electron trajectory, also the bulk plasmon mode at 3.8 eV can be excited.[11,24] However, as we mentioned in the Method section we have chosen not to include the bulk contribution. For the gap center trajectory (lower spectra), the bonding dipolar dimer mode cannot be excited and the spectrum is dominated by the antibonding dipolar LSPR.[11,23,24] Incidentally, due to retardation effects the position of this mode is slightly different for the different excitation configurations. This spectral shift has been observed experimentally for dimers of large nanoparticles.[24]

SUPPORTED NANOSTRUCTURES

EELS experiments require very thin nonabsorbing substrates to minimize energy losses. Typical EELS substrates are made of mica, silica (SiO_2), silicon nitride (Si_3N_4, SiN_x), or carbon (C), and their thickness generally ranges from 5 to 50 nm. Even though such thin substrates introduce a negligible EELS background and are often considered to have a negligible effect on the optical properties of the supported nanostructure (i.e., small spectral shift with respect to the free-standing nanostructure), they can be crucial in some situations.[41] For this reason, we calculate the EELS spectra for gold nanodisks of diameter a = 50 nm and height h = 15 nm placed on 30 nm thick substrates of different dielectric permittivities: ε = 1 (free-standing); ε = 2 (SiO_2);[42,43] and ε = 4 (Si_3N_4).[42,44] As in the case of the isolated sphere, we use the gold dielectric function tabulated by Johnson and Christy[35] in the BEM calculations and MCMs fit of the later in the FDTD calculations (Supporting Information, S2). The FDTD simulation parameters are the same as in previous cases (cf. Supporting Information, S3), and the electron velocity is set to v = 0.5c (i.e., 80 keV). The results are shown in Figure 4 for FDTD (blue lines) and BEM (red lines) for an impact parameter b = 27 nm (in close proximity to the nanodisk). As expected, the dipolar LSPR (2.3 eV for ε = 1) red-shifts with increasing permittivity of the substrate (1.97 eV for ε = 4). Interestingly, it has to be noticed a change in the LSPR line shape for ε = 4. This effect, along with the spectral shift clearly shows that even very thin substrates can have a significant impact on the EELS spectrum and may need to be included in the simulations.

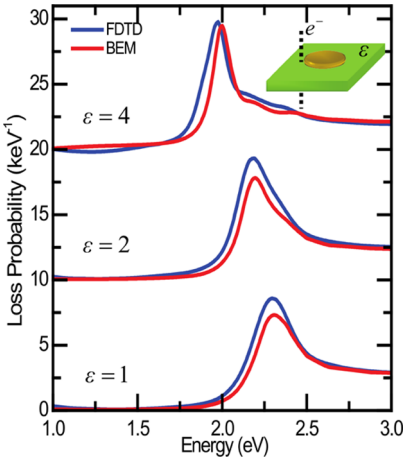

Figure 4. EELS spectra for a gold nanodisk of diameter a = 50 nm and height h = 15 nm placed on top of a 30 nm thick substrate with dielectric permittivity ε = 1, 2, and 4 calculated with the EELS-FDTD implementation (blue lines) and BEM (red lines). The impact parameter is fixed to b = 27 nm and the electron velocity is 0.5c (i.e., 80 keV).

Finally, to highlight the power and the flexibility of our EELS-FDTD implementation, we perform EELS calculations for a supported bowtie antenna. This complex structure is composed of two gold equilateral triangles with a lateral length a = 80 nm, a height h = 15 nm, separated by a gap g = 4 nm. The gold bowtie structure is placed on top of a 30 nm thick SiN substrate (calculations for other substrates are shown in Supporting Information, S7). We also include in the simulation a 2.5 nm chromium (Cr) adhesion layer. The dielectric permittivity of SiN is assumed to be constant and equal to 5.5,[45] while the corresponding one for Cr is described by MCMs fit of tabulated data (Supporting Information, S2).[39] The FDTD simulation parameters are given in Supporting Information, S3.

The results of this simulation are shown in Figure 5. There, we observe that for edge excitations (Figure 5a) the spectra

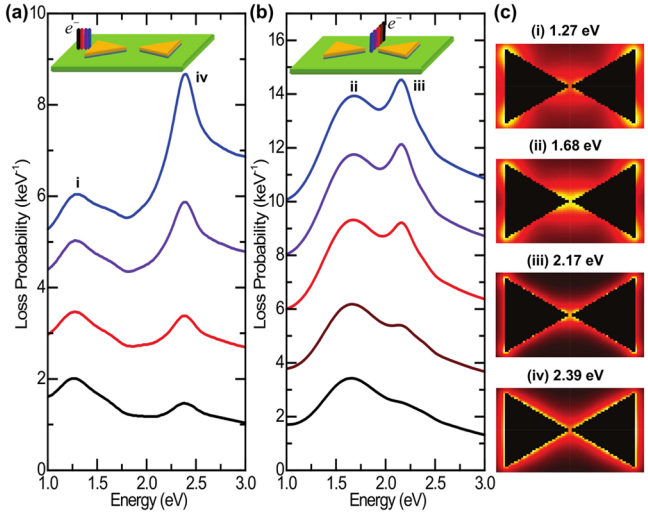

Figure 5. EELS spectra for a gold bowtie antenna calculated with the EELS-FDTD implementation. Each triangle has a lateral length a = 80 nm, height h = 15 nm, and gap g = 4 nm. The bowtie antenna is supported by a 30 nm thick SiN substrate. A 2.5 nm chromium adhesion layer is included. The electron velocity is taken equal to 0.5c (i.e., 80 keV) in all cases. (a) EELS spectra for edge excitation with four different impact parameters: 2 (blue), 5 (purple), 10 (red), and 15 nm (black; cf. inset). (b) EELS spectra for gap excitation with five different impact parameters: 0 (blue), 2 (purple), 5 (red), 10 (brown), and 15 nm (black; cf. inset). (c) EELS maps calculated at (i) 1.27, (ii) 1.68, (iii) 2.17, and (iv) 2.39 eV.

display two LSPRs (i, iv) located at 1.27 and 2.39 eV, respectively. In this case, different impact parameters produce very different intensity ratios for these LSPRs. On the other hand when electron trajectory crosses the center of the gap (Figure 5b) the EELS spectrum displays two distinct LSPRs (ii, iii) at 1.68 and 2.17 eV, respectively, with relative intensities that are much less dependent on the impact parameter. When displacing the electron trajectory off-axis, the LSPR at 2.17 eV (iii) becomes weaker progressively, while the one at 1.68 eV (ii) remains unchanged. All these results, along with the results for a single triangular prism (Supporting Information, S8), are in good agreement with the experimental observations by Yang and co-workers.[10,12] The small discrepancies, mainly in the line widths, are related to the presence of a thicker Cr adhesion layer in our calculations, which is known to introduce a

DOI: 10.1021/ph500408e
ACS Photonics 2015, 2, 369−375

broadening and a red-shift of the LSPRs (cf. Supporting Information, S8).[46,47]

Figure 5c shows the EELS maps corresponding to the four LSPRs (i–iv) calculated using our EELS-FDTD implementation with a 2 nm spatial resolution. Similarly to the dimer, we here choose to exclude penetrating trajectories. The nature of the LSP modes can straightforwardly be determined from these maps. Modes (i) and (ii) correspond to the dipolar bonding (bright) and antibonding (dark) modes, respectively. The map for 2.39 eV shows strong EELS signal from each bowtie edge underlining the high-order nature of mode (iv). These results are also in excellent quantitative agreement with the recent studies by Yang and co-workers.[10,12] Finally, mode (iii) displays a EELS signal which is strongly localized at the bowtie gap. This spatial confinement directly correlates with the rapid vanishing of mode (iii) when the electron trajectory is displaced off-gap (Figure 5b). Interestingly, this mode was not imaged by Duan et al. because their excitation geometry was off-gap excitation.[10]

CONCLUSIONS

We have presented a simple procedure to calculate the energy loss probability of fast electrons interacting with metallic nanostructures. Although this method can be implemented with any Maxwell's equation solver we have chosen here to work with the commercial package Lumerical FDTD Solutions[29] due to the flexibility of the FDTD method and its user-friendly environment. Contrary to most of the well-established methods, we have shown that this implementation can deal with both penetrating and nonpenetrating trajectories and nanostructures of arbitrary geometries and morphologies, including substrates and adhesion layers. We have benchmarked our EELS-FDTD implementation by comparing the results with the well-established BEM method for different representative nanostructures, such as nanospheres, nanoparticle dimers, and a nanodisk supported by a substrate. Furthermore, we have applied this method to study the EELS spectrum of a complex system consisting of a supported bowtie antenna, and we have mapped the LSPR modes of the latter. Our EELS-FDTD method provides a simple and convenient approach for the calculation of EELS spectra and maps from complex nanostructures of arbitrary shape and composition.

ASSOCIATED CONTENT

Supporting Information

(S1) Lumerical and Matlab scripts for postprocessing and EELS spectrum computation. (S2) Dielectric function of metals: Multicoefficient models in FDTD. (S3) Convergence of the EELS spectra: FDTD Lumerical parameters. (S4) Computational resource: EELS-FDTD versus BEM versus e-DDA. (S5) Penetrating trajectory: Numerical error and workaround. (S6) Convergence of the EELS spectra: Electron path meshing. (S7) EELS spectra of a bowtie antenna: Substrate effect. (S8) EELS spectra of a single gold triangular prism: Effect of the Cr layer. This material is available free of charge via the Internet at http://pubs.acs.org.

AUTHOR INFORMATION

Corresponding Authors

*E-mail: alejandro.manjavacas@rice.edu.
*E-mail: nicolas.large@northwestern.edu.
*E-mail: nordland@rice.edu.

Present Address

[‖]Department of Chemistry, Northwestern University, Evanston, IL, United States (N.L.).

Notes

The authors declare no competing financial interest.

ACKNOWLEDGMENTS

The authors thank F. J. García de Abajo for his insight and stimulating discussions. This work was supported by the Robert A. Welch Foundation under Grant C-1222, the Cyberinfrastructure for Computational Research funded by NSF under Grant CNS-0821727, and by the Data Analysis and Visualization Cyberinfrastructure under NSF Grant OCI-0959097. A.M. acknowledges support from the Welch Foundation under the J. Evans Attwell-Welch Fellowship for Nanoscale Research, administrated by the Richard E. Smalley Institute for Nanoscale Science and Technology (Grant L-C-004).

REFERENCES

(1) Ritchie, R. H. Plasma losses by fast electrons in thin films. *Phys. Rev.* **1957**, *106*, 874.
(2) Powell, C. J.; Swan, J. B. Origin of the characteristic electron energy losses in aluminum. *Phys. Rev.* **1959**, *115*, 869.
(3) Watanabe, H. Experimental evidence for the collective nature of the characteristic energy loss of electrons in solids: studies on the dispersion relation of plasma frequency. *J. Phys. Soc. Jpn.* **1956**, *11*, 112.
(4) Pettit, R. B.; Silcox, J.; Vincent, R. Measurement of surface-plasmon dispersion in oxidized aluminum films. *Phys. Rev. B* **1975**, *11*, 3116–3123.
(5) Botton, G. Probing bonding and electronic structure at atomic resolution with spectroscopic imaging. *MRS Bull.* **2012**, *37*, 21.
(6) Kociak, M.; Stéphan, O. Mapping plasmons at the nanometer scale in an electron microscope. *Chem. Soc. Rev.* **2014**, *43*, 3865–3883.
(7) García de Abajo, F. J.; Kociak, M. Probing the photonic local density of states with electron energy loss spectroscopy. *Phys. Rev. Lett.* **2008**, *100*, 106804.
(8) García de Abajo, F. J.; Kociak, M. Electron energy-gain spectroscopy. *New J. Phys.* **2008**, *10*, 073035.
(9) García de Abajo, F. J. Optical excitations in electron microscopy. *Rev. Mod. Phys.* **2010**, *82*, 209.
(10) Duan, H.; Fernández-Domínguez, A. I.; Bosman, M.; Maier, S. A.; Yang, J. K. W. Nanoplasmonics: Classical down to the nanometer scale. *Nano Lett.* **2012**, *12*, 1683.
(11) Koh, A. L.; Bao, K.; Kahn, I.; Smith, W. E.; Kothleitner, P.; Nordlander, G.; Maier, S. A.; McComb, D. W. Electron energy-loss spectroscopy (EELS) of surface plasmons in single silver particle and dimers: Influence of beam damage and mapping of dark modes. *ACS Nano* **2009**, *3*, 3015.
(12) Koh, A. L.; Fernández-Domínguez, A. I.; McComb, D. W.; Maier, S. A.; Yang, J. K. W. High-resolution mapping of electron-beam-excited plasmon modes in lithographically defined gold nanostructures. *Nano Lett.* **2011**, *11*, 1323–1330.
(13) Barrow, S. J.; Rossouw, D.; Funston, A. M.; Botton, G. A.; Mulvaney, P. Mapping bright and dark modes in gold nanoparticle chains using electron energy loss spectroscopy. *Nano Lett.* **2014**, *14*, 3799–3808.
(14) Bosman, M.; Ye, E.; Tan, S. F.; Nijhuis, C. A.; Yang, J. K. W.; Marty, R.; Mlayah, A.; Arbouet, A.; Girard, C.; Han, M.-Y. Surface plasmon damping quantified with an electron nanoprobe. *Sci. Rep.* **2013**, *3*, 1312.
(15) García de Abajo, F. J.; Howie, A. Retarded field calculation of electron energy loss in inhomogeneous dielectrics. *Phys. Rev. B* **2002**, *65*, 115418.
(16) Hohenester, U. Simulating electron energy loss spectroscopy with the MNPBEM toolbox. *Comput. Phys. Commun.* **2014**, *185*, 1177.

DOI: 10.1021/ph500408e
ACS Photonics 2015, 2, 369–375

(17) Geuquet, N.; Henrard, L. EELS and optical response of a noble metal nanoparticle in the frame of a discrete dipole approximation. *Ultramicroscopy* **2010**, *110*, 1075.
(18) Bigelow, N.; Vaschillo, A.; Iberi, V.; Camden, J. P.; Masiello, D. Characterization of the electron- and photon-driven plasmonic excitations of metal nanorods. *ACS Nano* **2012**, *6*, 7497.
(19) Bigelow, N.; Vaschillo, A.; Camden, J. P.; Masiello, D. Signatures of Fano interferences in the electron energy loss spectroscopy and cathodoluminescence of symmetry-broken nanorod dimers. *ACS Nano* **2013**, *7*, 4511.
(20) Reed, N. W.; Chen, J. M.; MacDonald, N. C.; Silox, J.; Bertsch, G. F. Fabrication and STEM/EELS measurements of nanometer-scale silicon tips and filaments. *Phys. Rev. B* **1999**, *60*, 5641.
(21) Talebi, N.; Sigle, W.; Vogelsang, R.; van Aken, P. Numerical simulations of interference effects in photon-assisted electron energy-loss spectroscopy. *New J. Phys.* **2013**, *15*, 053013.
(22) Matyssek, C.; Niegemann, J.; Hergert, W.; Busch, K. Computing electron energy loss spectra with the discontinuous Galerkin time-domain method. *Photon. Nanostruct.: Fundam. Appl.* **2011**, *9*, 367.
(23) Song, F.; Wang, T.; Wang, X.; Xu, C.; He, L.; Wan, J.; van Haesendonck, C.; Ringer, S. P.; Han, M.; Liu, Z.; Wang, G. Visualizing plasmon coupling in closely spaced chains of Ag nanoparticles by electron energy-loss spectroscopy. *Small* **2010**, *6*, 446.
(24) Kadkhodazadeh, S.; Wagner, J. B.; Joseph, V.; Kneipp, J.; Kneipp, H.; Kneipp, K. Electron energy loss and one- and two-photon excited SERS probing of hot plasmonic silver nanoaggregates. *Plasmonics* **2013**, *2*, 763.
(25) Scholl, J. A.; Koh, A. L.; Dionne, J. A. Quantum plasmon resonances of individual metallic nanoparticles. *Nature* **2012**, *483*, 421.
(26) Chaturvedi, P.; Hsu, K. H.; Kumar, A.; Fung, K. H.; Mabon, J. C.; Fang, N. X. Imaging of plasmonic modes of silver nanoparticles using high-resolution cathodoluminescence spectroscopy. *ACS Nano* **2009**, *3*, 2965−2974.
(27) Das, P.; Chini, T. K.; Pond, J. Probing higher order surface plasmon modes on individual truncated tetrahedral gold nanoparticle using cathodoluminescence imaging and spectroscopy combined with FDTD simulations. *J. Phys. Chem. C* **2012**, *116*, 15610.
(28) Das, P.; Kedia, A.; Kumar, P. S.; Large, N.; Chini, T. K. Local electron beam excitation and substrate effect on the plasmonic response of single gold nanostars. *Nanotechnology* **2013**, *24*, 405704.
(29) Lumerical Solutions, Inc.; http://www.lumerical.com/tcad-products/fdtd/.
(30) Yee, K. Numerical solution of initial boundary value problems involving Maxwell's equations in isotropic media. *IEEE Trans. Antennas Propag.* **1966**, *14*, 302.
(31) García de Abajo, F. J.; Howie, A. Relativistic electron energy loss and electron-induced photon emission in inhomogeneous dielectrics. *Phys. Rev. Lett.* **1998**, *80*, 5180−5183.
(32) García de Abajo, F. J. Relativistic energy loss and induced photon emission in the interaction of a dielectric sphere with an external electron beam. *Phys. Rev. B* **1999**, *59*, 3095−3107.
(33) Novotny, L., Hecht, B. *Principles of Nano-Optics*, 1st ed.; Cambridge University Press: New York, 2006.
(34) Bérenger, J.-P. Perfectly Matched Layer (PML) for Computational Electromagnetics. *Synthesis Lectures on Computational Electromagnetics* **2007**, *2*, 1−117 DOI: 10.2200/S00030ED1V01Y200605-CEM008.
(35) Johnson, P. B.; Christy, R. Optical constants of the noble metals. *Phys. Rev. B* **1972**, *6*, 4370.
(36) Myroshnychenko, V.; Rodríguez-Fernández, J.; Pastoriza-Santos, I.; Funston, A. M.; Novo, C.; Mulvaney, P.; Liz-Marzán, L. M.; García de Abajo, F. J. Modelling the optical response of gold nanoparticles. *Chem. Soc. Rev.* **2008**, *37*, 1792−1805.
(37) Kadkhodazadeh, S.; Wagner, J. B.; Kneipp, H.; Kneipp, K. Coexistence of classical and quantum plasmonics in large plasmonic structures with subnanometer gaps. *Appl. Phys. Lett.* **2013**, *103*, 083103.
(38) Kadkhodazadeh, S.; de Lasson, J. R.; Beleggia, M.; Kneipp, H.; Wagner, J. B.; Kneipp, K. Scaling of the surface plasmon resonance in gold and silver dimers probed by EELS. *J. Phys. Chem. C* **2014**, *118*, 5478−5485.
(39) Palik, E. D., Ed. *Handbook of Optical Constants of Solids*; Academic Press: New York, 1985; Vol. *1*.
(40) Nordlander, P.; Oubre, C.; Prodan, E.; Li, K.; Stockman, M. I. Plasmon hybridization in nanoparticle dimers. *Nano Lett.* **2004**, *4*, 899−903.
(41) Knight, M. W.; Wu, Y. P.; Lassiter, J. B.; Nordlander, P.; Halas, N. J. Substrates matter: Influence of an adjacent dielectric on an individual plasmonic nanoparticle. *Nano Lett.* **2009**, *9*, 2188.
(42) Bååk, T. Silicon oxynitride; a material for GRIN optics. *Appl. Opt.* **1982**, *21*, 1069−1072.
(43) Gao, L.; Lemarchand, F.; Lequime, M. Refractive index determination of SiO_2 layer in the UV/vis/NIR range: Spectrophotometric reverse engineering on single and bilayer designs. *J. Eur. Opt. Soc.* **2013**, *8*, 13010.
(44) Philipp, H. R. Optical properties of silicon nitride. *J. Electrochem. Soc.* **1973**, *120*, 295−300.
(45) Tanaka, M.; Saida, S.; Tsunashima, Y. Film properties of lowk silicon nitride films formed by hexachlorodisilane and ammonia. *J. Electrochem. Soc.* **2000**, *147*, 2284−2289.
(46) Vial, A.; Laroche, T. Description of dispersion properties of metals by means of the critical points model and application to the study of resonant structures using the FDTD method. *J. Phys. D: Appl. Phys.* **2007**, *40*, 7152−7158.
(47) Zheng, Y. B.; Juluri, B. K.; Mao, X.; Walker, T. R.; Huang, T. J. Systematic investigation of localized surface plasmon resonance of long-range ordered Au nanodisk arrays. *J. Appl. Phys.* **2008**, *103*, 014308.

DOI: 10.1021/ph500408e
ACS Photonics 2015, 2, 369−375